Research papers

Stratified flow over complex topography: A model study of the bottom drag and associated mixing

Knut S. Seim [a,*], Ilker Fer [b], Helge Avlesen [c]

[a] Department of Marine Technology, Norwegian University of Science and Technology, O. Nielsens vei 10, Tyholt, 7491 Trondheim, Norway
[b] Geophysical Institute, University of Bergen, Allégaten 70, 5007 Bergen, Norway
[c] Bergen Center for Computational Science, Uni Research, Thormohlensgate 55, 5008 Bergen, Norway

ARTICLE INFO

ABSTRACT

The flow of stratified fluid over complex topography may lead to a significant drag on the fluid, exerted by the bottom obstacles. Using a 2-m resolution, three-dimensional, non-hydrostatic numerical ocean model, the drag and associated mixing on a stratified flow over real, 1-m resolution topography (interpolated to model resolution) is studied. With a typical mountain height of 12 m in 174 m water and buoyancy frequencies ranging from 0.6×10^{-2} s^{-1} to 1.2×10^{-2} s^{-1}, resolving the topographic features leads to extensive drag exerted on the flow manifested through three different processes: (i) gravity wave drag, (ii) aerodynamic or blocked flow drag, and (iii) hydraulic drag. A parameterization of the internal wave drag based on linear, two-dimensional, hydrostatic wave solutions provides satisfactory results in terms of the turbulent kinetic energy levels. The depth of the layer where the vertical momentum flux is deposited, however, is underestimated, leading to an overestimated gravity wave drag in the layer.

1. Introduction

Understanding the boundary layer processes in the ocean is essential for an accurate representation of the vertical buoyancy flux in ocean general circulation models. In order to close the overturning circulation, the dense water masses sinking to abyssal depths across all major ocean basins have to be balanced by a buoyancy gain and an upward vertical motion. In the interior of the ocean, diapycnal mixing is the only mechanism that can increase the buoyancy of a water parcel (Gregg, 1987). Observations indicate a strong association between diapycnal mixing in the abyss and rough topography (Polzin et al., 1997; Ledwell et al., 2000), and that the abyssal circulations have complex spatial structures that are linked to the underlying bathymetry (Thurnherr, 2006). Bottom attached, dense overflows and their mixing with ambient waters (diapycnal mixing) are strongly influenced by complex topography. Understanding and parameterizing the mechanisms leading to mixing of stratified flow over topography is important to properly understand the overturning circulation.

It has been recognized that overflows are not necessarily homogeneous, but may have a vertical density structure, typically consisting of a well-mixed dense bottom layer and a stratified interfacial layer (Peters and Johns, 2005; Fer et al., 2010; Seim et al., 2010), in which internal waves can contribute to mixing (Seim and Fer, 2011). Internal wave breaking is suggested to be the dominating mechanism for dissipation of turbulent energy in the ambient water above the Faroe Bank Channel overflow plume and its contribution to mixing in the interfacial layer should not be ignored (Seim and Fer, 2011). This mechanism is typically neither resolved nor parameterized in numerical model studies of such overflows due to the scale of typical overflow regions (and consequently coarse resolution of numerical models) and the lack of internal wave mixing parameterization in local turbulence closure schemes. The models only account for bottom roughness through simple drag laws. Parameterizations of mountain wave drag based on linear internal wave solutions have significantly improved the atmospheric general circulation models (Kim and Arakawa, 1995). In most ocean models, on the other hand, due to the lack of high resolution topographic data and limited knowledge of the interaction between topographic features and the bottom boundary layer, the effect of sub-grid-scale topographic features is not parameterized. Klymak and Legg (2010) presented a numerical mixing scheme that enhances mixing and viscosity in the presence of breaking internal waves, but the scheme requires that the breaking internal waves are relatively well resolved by the model. Bottom topography can affect the momentum budget of the ocean, without requiring significant turbulence fluxes, through pressure drag and internal wave propagation with wave

dissipation possibly occurring some distance from the source region (Skyllingstad and Wijesekera, 2004).

In this study we employ a high resolution (comparable to the typical length scale of turbulent overturns) and non-hydrostatic numerical ocean model to investigate the flow of stratified fluid over complex topography. The high resolution, non-hydrostatic model is essential to resolve the overturning internal waves induced by the complex topography (Xing and Davies, 2006; Berntsen et al., 2009). The aim of this study is to test a parameterization of the wave drag on the flow exerted by unresolved topography, with known characteristics in our case, and consequently test its ability to represent the wave drag from sub-grid-scale topography in models with coarse resolution, or where the resolution of the topographic data is inadequate. The background theory is given in Section 2 for homogeneous and stratified flow over topography. The numerical model and the model set-up are described in Section 3, followed by the results presented and discussed in Section 5. Conclusions are drawn at Section 6.

2. Background

2.1. Homogeneous fluid flow

The first step in studying flow over topography is to consider the flow of a homogeneous layer past isolated topography (Baines, 1995, Chapter 2). Such single layer flows are typically characterized by the Froude number of the undisturbed flow defined by $F_0 = U/\sqrt{gd_0}$, where U is the horizontal velocity, g is the gravitational acceleration, and d_0 is the undisturbed flow depth. The critical Froude number is defined as $F_0 = 1$, i.e. when the flow speed equals the phase speed of long gravity waves. In sub-critical flows ($F_0 < 1$), linear long gravity waves may propagate both upstream and downstream, whereas in super-critical flows ($F_0 > 1$) the upstream propagation is not possible. For the one-dimensional flow there is only an associated drag force on the obstacle in the resonant case when $F_0 = 1$ (critical flow), and the upstream propagating wave remains stationary relative to the obstacle. In the two-dimensional case, there is no drag force on the obstacle for $F_0 < 1$, but a discontinuously increasing drag as F_0 increases above unity (Baines, 1995). In this hydraulic flow theory it is assumed that the flow is hydrostatic, which is a good approximation for obstacles with a long horizontal scale compared to the fluid depth such that $d_0/L \ll 1$, where L is the obstacle width, or $kd_0 \ll 1$, where k is the wave-number. For the values of $kd_0 \gg 1$, the flow generates dispersive, non-hydrostatic waves that propagate energy away from the obstacle. In general, this condition is not atypical in the ocean, particularly when considering regional scale flows such as the flow of dense overflow water over rough topography or through channel systems.

2.2. Stratified flow

The above hydraulic theory is no longer applicable when the flow is stratified (due to propagating internal waves). Assuming a stable, undisturbed flow, any small disturbance may extract energy from the kinetic energy of the mean flow, generating a spectrum of internal wave modes. In particular breaking internal waves may be generated when topography is introduced. If the aspect ratio, h/a where h is the height of an obstacle and a is the half-width, of the obstacle is sufficiently large (typically h/a larger than 0.1–1.0 depending on the stratification), overturning lee waves leading to increased mixing are expected (Baines, 1995; Xing and Davies, 2011). In a flow limited with depth d_0, two significant dimensionless quantities are the vertical mode number,

$$K = \frac{Nd_0}{\pi U}, \tag{1}$$

and the dimensionless obstacle height,

$$h_n = \frac{Nh}{U}, \tag{2}$$

where

$$N = \sqrt{-\frac{g}{\rho_0}\frac{\partial \rho}{\partial z}} \tag{3}$$

is the buoyancy frequency, h is the height of the obstacle, ρ is the density and ρ_0 is a constant reference density. The dimensionless obstacle height is the ratio of the vertical extent of the obstacle to the approximate vertical length scale of the waves, U/N, and is thus a measure of the non-linearity of the disturbed flow. As h_n increases, the flow is more likely to generate overturning and breaking internal waves. The critical limit, where breaking of the internal waves commences, of the non-dimensional obstacle height, h_{nc}, depends on the shape of the obstacle. In a study of obstacles of general semi-elliptical shape over the whole range of aspect ratios $\gamma = h_m/a$, where h_m is the maximum obstacle height and a is the half-width of the obstacle, Huppert and Miles (1969) found h_{nc} to range from 0.67 ($\gamma = 0$; flat semi-ellipse) to 1.73 ($\gamma = \infty$; vertical barrier). Long (1955) derived a non-linear stream-function equation for a uniform infinite-depth flow over a bump and predicted $h_{nc} = 1.27$ for a semi-circle ($\gamma = 1$). In a more recent numerical study, Lamb (1994) found h_{nc} (for $1 < K < 2$) was considerably smaller than that predicted by Long's model.

For depth-limited flow the additional length-scale d_0 is introduced through the vertical mode number K, which can also be interpreted as one-half of the inverse Froude number with respect to the fastest internal wave mode with phase speed $c_0 = \pm 2Nd_0/\pi$ relative to the fluid (Baines, 1995). When $K < 1$ (supercritical flow) linear theory gives a reasonably accurate description of the flow, in good agreement with observations (Baines, 1979). In this case the obstacle exerts no significant drag on the flow. For flows with $K > 1$ (sub-critical flow), observations and numerical studies have concentrated in the range where only the first lee wave mode is present, i.e. $1 < K < 2$. The linear theory describes the lee wave field reasonably well as long as $h_n \ll 1$, and K is not close to an integer; if $K=j$ for a positive integer j, the mean flow is critical with respect to the jth mode in the long wave length limit, see Baines (1995). For steady flows with $K \neq j$, the pressure distribution over the obstacle is symmetric and the drag vanishes, while for $K=j$ the upstream propagating part and the steady part of the jth mode internal wave are in resonance, and the drag is non-zero as in the homogeneous layer case.

Performing three-dimensional large-eddy simulations of a stratified oceanic flow over topography with a "witch of Agnesi" profile with mode numbers (K) ranging from 0.89 to 2.24, Skyllingstad and Wijesekera (2004) obtained qualitatively similar results to the analytical and laboratory results of Long (1955) and Baines (1979). They found a strong dependence on both the mode number and the relative obstacle height when a free-slip condition on the lower boundary was used. Introducing a bottom frictional drag decreased the role of lee waves and the accompanying wave drag in some cases, especially for large velocities (small K). Skyllingstad and Wijesekera's (2004) results were also in agreement with Lamb (1994) in showing that obstacle height thresholds for wave breaking based on Long's equation were too high.

2.3. Stratified flow over complex terrain

Proceeding to the more realistic case of three-dimensional topography, the distinction between finite and infinite depth is

less significant as the disturbances caused by a topographic feature spread out laterally as well as vertically so that the presence of an upper boundary has a minor effect locally (unless it is at a low level) (Baines, 1995). If the obstacles in a complex region all have comparable heights with $Nh/U < 1$, the disturbance field of each obstacle is approximately linear and the interaction is minimal. In this case the drag is transmitted in the form of internal gravity waves. The reference-level drag, τ_0, and the drag above the reference level, τ, may be expressed as (Palmer et al., 1986; Kim and Arakawa, 1995)

$$\tau_0 = \kappa \rho_0 N_0 U_0 h^2, \tag{4}$$

$$\tau = \kappa \rho N U \delta h^2, \tag{5}$$

where κ is a tunable constant dependent on the statistical properties of the topography, h is a height proportional to the standard deviation of the topography, δh is the displacement wave amplitude, and ρ_0, N_0 and U_0 are the low-level reference density, buoyancy frequency, and the velocity component in the direction of the reference drag. The low-level parameters are typically evaluated between the blocking height $z_b \approx h - U/N$ and the representative obstacle height h. If, on the other hand, $Nh/U > 1$ flow splitting and lee wave overturning occur. The interaction between disturbances induced by individual obstacles may be significant and the drag by the complex terrain is spread amongst three different processes: gravity wave drag (Eqs. (4) and (5)), hydraulic drag associated with hydraulic flow over the topography, and aerodynamic or blocked flow drag. Linear theory may, however, still be applied if the obstacles are relatively isolated and spread out, by the linear superposition of the net effects of each obstacle and its wake (Baines, 1995). In this study we focus on the gravity wave drag, and discuss blocked flow drag and hydraulic drag where appropriate.

3. The numerical model and set-up

The numerical model used in this study is the Bergen Ocean Model (BOM, Berntsen, 2000). BOM is a σ-coordinate (terrain-following) ocean model with non-hydrostatic capability. The standard second-order Princeton Ocean Model (POM) method is applied to estimate the internal pressure gradients (Blumberg and Mellor, 1987; Mellor, 1996). For advection of momentum and density a TVD-scheme with a superbee limiter described in Yang and Przekwas (1992) is applied. The model is mode split with a method similar to the splitting described in Berntsen et al. (1981) and Kowalik and Murty (1993). The solution is propagated in time using single time step methods. For the depth-integrated momentum and continuity equation a predictor–corrector method is applied.

3.1. Model set-up

The domain (Fig. 1) covers a 400 m × 400 m subregion of the Storegga slide region, on the continental slope west of mid-Norway. This region is selected due to its rough topography and the available high horizontal resolution (1 m) topography data collected in connection with the development of the Ormen Lange gas field. The original topographic data is truncated in the vertical to decrease the total depth and thus the time-step in the simulation. The model has a horizontal resolution of 2 m. In the vertical there are 81 layers, in 174 m water depth, resulting in a resolution of approximately 2 m (1.96–2.30 m). The boundaries at $y = 0$ m and $y = 400$ m are closed, while at both the inflow ($x = 0$ m) and outflow ($x = 400$ m) boundary, a flow relaxation scheme (FRS, Martinsen and Engedahl, 1987) is used. The FRS zone extends for 30 grid cells. To assure proper flux conservation in the domain, the topography is flattened
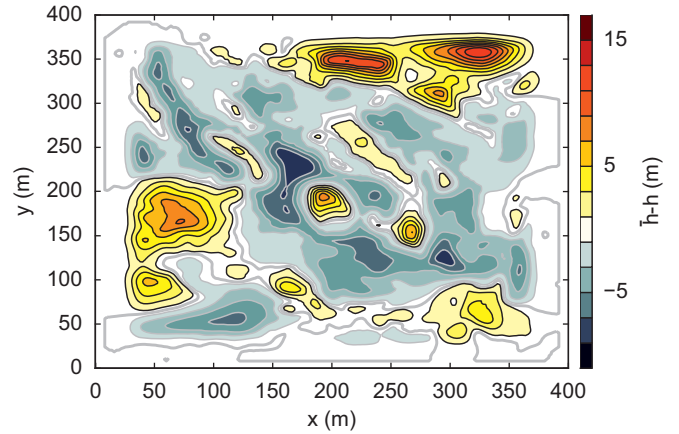

Fig. 1. Bottom topography illustrated as deviation from the mean depth. Positive deviations (crests) are contoured in warm colours and black lines, while negative deviations (troughs) are contoured in cool colours and grey lines. The white colour marks the interval between −1 and 1 m and the thick grey line is the zero contour.
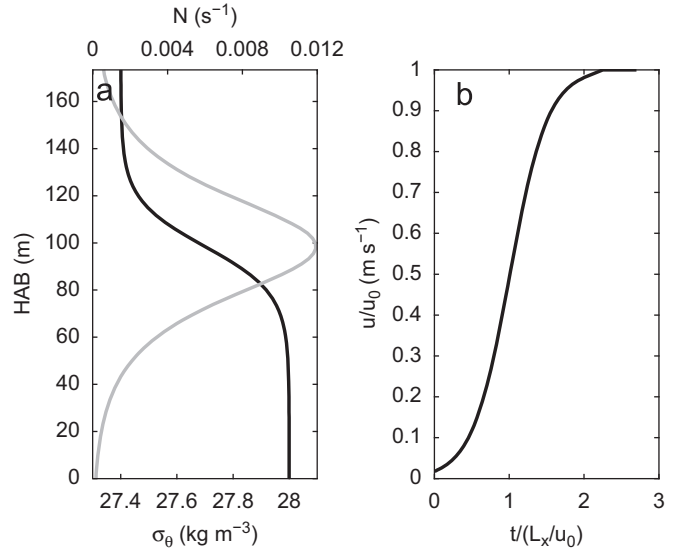

Fig. 2. (a) Initial hyperbolic tangent density (black) and buoyancy frequency (grey) profile, and (b) spin up of the inflow velocity with time toward the background velocity u_0. The spin-up time is non-dimensional and L_x is the length of the domain in the x-direction.

toward the boundaries with the first 5 cells set to the mean depth and a region of 25 cells where the topography is weighted by a hyperbolic tangent function.

Initially, the fluid is at rest. Two forms of stratification are studied: a linear density profile and a hyperbolic-tangent density profile resembling the Faroe Bank Channel overflow (Fer et al., 2010; Seim et al., 2010) with a well-mixed bottom layer and an interfacial layer of comparable thickness (Fig. 2). At the inflow boundary the velocity in the x-direction, u, is ramped up toward the background velocity u_0, over approximately twice the time a parcel needs to travel over the length of the domain, L_x, with the background velocity. The chosen ramp up period ensures a smooth transition to the background flow without introducing transients that can cause the model to run unstable. The density profile of the inflow water is set to either the linear or the hyperbolic-tangent density profile (Fig. 2a). Relaxation is applied for the surface elevation at the inflow boundary and for the surface elevation, density, and velocity at the outflow boundary to avoid contamination of the results by barotropic signals and reflection at the outflow boundary. The surface elevation at the

Table 1
Parameters for different model runs. For the hyperbolic-tangent (tanh) density profiles, the maximum value of the buoyancy frequency, N, is listed.

Run	$\rho(z)$	u_0 (m s^{-1})	N (s^{-1})	h_n	K
run1	Linear	0.1	5.7×10^{-3}	0.7	3.2
run2	Linear	0.1	1.0×10^{-2}	1.2	5.8
run3	tanh	0.1	1.2×10^{-2}	1.2[a]	5.4 (3.1[b])
run4[c]	tanh	0.1	1.2×10^{-2}	1.2	5.4 (3.1)
run5[d]	tanh	0.1	1.2×10^{-2}	1.2	5.4 (3.1)

[a] h_n is calculated where N is non-zero (50–100 m).
[b] If d_0 is taken to be the depth of the dense water (below 75 m).
[c] With turbulence closure.
[d] With turbulence closure and gravity wave drag parameterization.

inflow boundary is relaxed toward an average of the elevation in 30 grid cells (60 m) outside the FRS zone. At the outflow boundary, density is relaxed toward the average of 30 cells outside the FRS zone, while the velocity is relaxed toward the average over the domain omitting the FRS zones. The surface elevation is relaxed toward zero elevation at the outflow boundary. Due to the small extent of the domain we have ignored rotation in this study, i.e. $f=0$ where f is the Coriolis parameter, and thus these boundary conditions will ensure a steady background flow when the flow has settled after the initial ramp up of the velocity. The high resolution of the model partially resolves the turbulent overturns and allows for numerical stability even at weak viscosity. The background values of turbulent eddy diffusivity and viscosity are therefore kept low to allow the overturns develop in the model. The horizontal and vertical diffusivity is set to 1.0×10^{-6} m^2 s^{-1}, the horizontal viscosity is 1.0×10^{-4} m^2 s^{-1} and in the vertical the viscosity is 1.0×10^{-5} m^2 s^{-1}.

3.2. Model runs

The results presented in this study comprise of four different cases simulating flow over resolved complex terrain with varying stratification, and a fifth simulation in which the topography and drag are parameterized. In the last run, the domain represents one grid point region (GPR) with flat bottom, and the wave drag exerted on the flow is parameterized using the statistical properties of the resolved topography and the linear wave theory. The different simulation runs are listed in Table 1, and the high resolution topography is shown in Fig. 1. Initially the density is linear (run1 and run2) or a hyperbolic tangent profile (run3–5). The density and the corresponding buoyancy frequency profiles are shown in Fig. 2 together with the spin-up of the velocity identical for all cases. For the two linear density profile cases, the buoyancy frequency is 5.7×10^{-3} s^{-1} (run1) and 1.0×10^{-2} s^{-1} (run2).

4. Representation of topography

Considering our domain resembling one grid point in a coarse model with a depth given by the mean value of the 1-m resolution topography, $\overline{d}$, the sub-grid-scale topography of that GPR may be represented by four parameters: the variance μ^2 (μ is the standard deviation), the (an)isotropy parameter γ, the slope parameter (average of the local square gradient) σ, and θ giving the direction of most rapid variation. Analysing the Ormen Lange topography, Hove (2003) suggested a method of estimating these parameters which is adopted in this study. The vector field $\mathbf{m}(\mathbf{x})$

as a finite difference approximation to $\nabla d(\mathbf{x})$ is given by

$$\mathbf{m}(\mathbf{x}) = \left(\frac{d(\mathbf{x}+\Delta x)-d(\mathbf{x})}{\Delta x}, \frac{d(\mathbf{x}+\Delta y)-d(\mathbf{x})}{\Delta y} \right). \tag{6}$$

We then define the vector sum as

$$\mathbf{M} = \frac{1}{n}\sum_{\mathbf{x}} \frac{\mathbf{m}(\mathbf{x})}{|\mathbf{m}(\mathbf{x})|}, \tag{7}$$

where n is the number of grid points. Then the sub-grid-scale topography parameters are given by

$$\mu^2 = \frac{1}{A} \int \int (d-\overline{d})^2 \, dA, \tag{8a}$$

$$\gamma = \sqrt{1-|\mathbf{M}|}, \tag{8b}$$

$$\sigma = \frac{1}{n}\sum_{\mathbf{x}} |\mathbf{m}(\mathbf{x})|, \tag{8c}$$

$$\theta = \arctan\left(\frac{M_y}{M_x} \right). \tag{8d}$$

In Eq. (8d) M_x and M_y denote the x- and y-component, respectively, of the vector sum $\mathbf{M}$. For the domain in this study, the following parameter values are obtained: $\mu = 5.80$ m, $\sigma = 0.56$, $\gamma = 0.94$ and $\theta = 1.35$ rad. Using μ, σ, γ and θ, an obstacle representative of the entire GPR topography can be obtained with height 2μ and known shape and orientation (σ, γ, and θ). The actual topography can now be conceptually replaced by repetitions of this representative obstacle within the computational domain. The problem of specifying the effect of the complex terrain on the flow reduces to specifying the effect of this single obstacle, see e.g. Baines (1995, Chapter 7).

5. Results and discussion

5.1. Drag states

Domain-integrated kinetic ($\mathcal{E}_k$), available potential ($\mathcal{E}_{ap}$), potential ($\mathcal{E}_p$) and background potential ($\mathcal{E}_{ps}$) energies have been calculated following Molemaker and McWilliams (2010):

$$\mathcal{E}_k = \int_V E_k \, dx \, dy \, dz, \tag{9a}$$

$$\mathcal{E}_p = \int_V E_p \, dx \, dy \, dz, \tag{9b}$$

$$\mathcal{E}_{ps} = \int_V E_{ps} \, dx \, dy \, dz, \tag{9c}$$

$$\mathcal{E}_{ap} = \int_V E_{ap} \, dx \, dy \, dz, \tag{9d}$$

where the energy densities are defined as

$$E_k = \tfrac{1}{2}(u^2 + v^2 + w^2), \tag{10a}$$

$$E_p = zb, \tag{10b}$$

$$E_{ps} = z\overline{b}_s, \tag{10c}$$

$$E_{aps} = \frac{(b_s - \overline{b}_s)^2}{2\delta_z \overline{b}_s}, \tag{10d}$$

$$E_{ap} = E_p - E_{ps} + E_{aps}. \tag{10e}$$

Here $b = g(1-\rho/\rho_0)$ is the buoyancy field proportional to the density ρ, b_s is the buoyancy field resulting from sorting the density field following a technique proposed by Winters et al. (1995), and δ_z

denotes vertical differential operator. A sorting algorithm is applied assigning the densest fluid to the grid boxes with the lowest vertical coordinate. Following Molemaker and McWilliams (2010), the available potential energy of the sorted buoyancy field is added in the calculation of E_{ap} to correct for the deviation of the available potential energy of the sorted field (dependent on the grid)
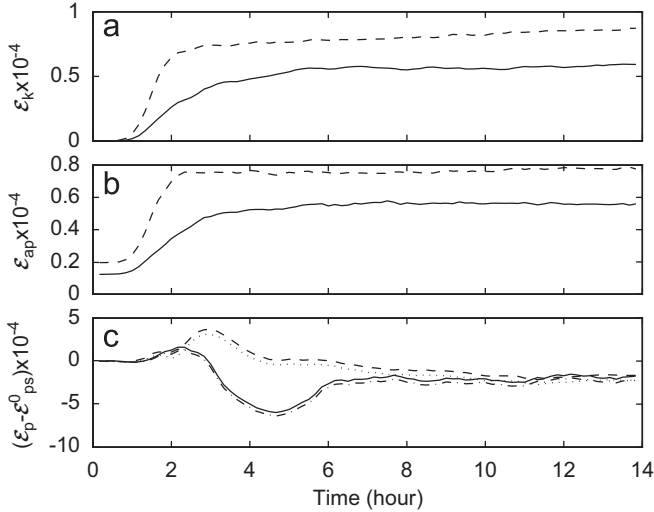
from a horizontally uniform profile. The overbar denotes a horizontal average.

The model was run for 14 h until the energy stabilizes with time so that the dynamics is not dominated by the external forcing of the model. The time evolution of the domain-integrated energetics is shown in Fig. 3 for both the linear (run1) and the hyperbolic-tangent (run3) density profiles. The kinetic energy and the available potential energy stabilize within 3 h after the spin-up of the velocity, while the potential energy needs longer time to stabilize due to the different outflow boundary condition on the density field. The results from a 2-h period between 8.5 and 10.5 h is selected for further investigation.

The time average of the velocity normalized by u_0 along a section at $y = 200$ m is shown for run1–run3 in Fig. 4, together with the density fields. In all the cases the potential density surfaces and the horizontal velocity field are significantly affected by the topography. The maximum velocities are 0.20 m s^{-1}, 0.15 m s^{-1}, and 0.17 m s^{-1} for run1, run2, and run3, respectively, and the minimum velocities are -0.05 m s^{-1}, -0.05 m s^{-1}, and -0.07 m s^{-1}. The only difference between the three cases is the stratification which has a major impact on the wave/non-wave regime of the flow, and affects the velocity maxima and the drag exerted in the water column.

Different from run2 and 3, the constant buoyancy frequency in run1 is such that the non-dimensional height is less than unity (Table 1), and the flow is expected to be linear, with no overturning internal waves. To generate propagating waves, according to the linear theory of two-dimensional waves, the intrinsic frequency of the waves (U/L) must be smaller than the buoyancy frequency. This leads to a limit on the horizontal length scale of
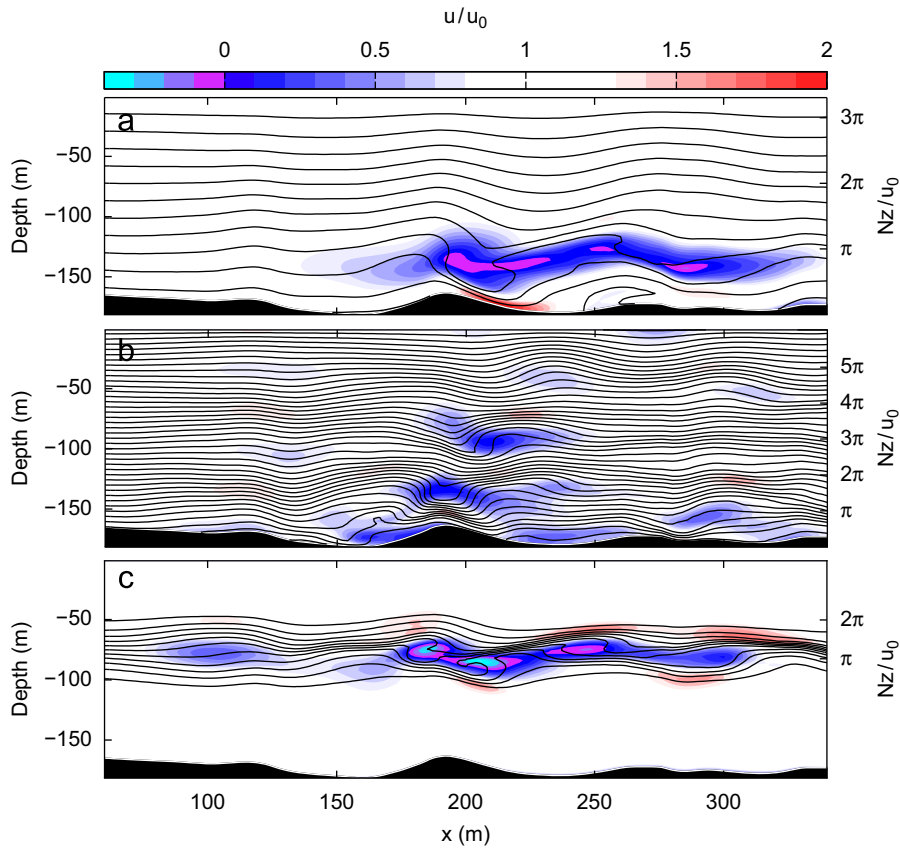

Fig. 3. Time evolution of the domain integrated (a) kinetic energy ($\mathcal{E}_k$), (b) available potential energy ($\mathcal{E}_{ap}$) and (c) potential energy ($\mathcal{E}_p$) relative to the initial background potential energy ($\mathcal{E}_{ps}^0$), for run1 (dashed) and run2 (solid). In (c) background potential energy ($\mathcal{E}_{ps}$) relative to $\mathcal{E}_{ps}^0$ is also shown (run1, dotted; run3, dash-dot).

Fig. 4. Vertical cross section of potential density and the horizontal velocity, u, normalized by u_0 for (a) run1, (b) run2, and (c) run3, at $y = 200$ m averaged over the period from approximately 8.5 to 10.5 h. For (a) and (b), with N = constant, the vertical axis on the right is the vertical phase of a linear wave solution with vertical wave number $k = N/u_0$. The profile of Nz/u_0 is shown for (c). Density contours are drawn at 0.05 kg m^{-3} intervals. The obstacle at approximately $x = 200$ m is the only obstacle exceeding the critical limit in run1.

the topography, $L > 2\pi N/U$, approximately 110 m for run1 and 60 m and 50 m for run2 and run3, respectively, using the background velocity u_0. This calculation supports the difference seen between run1 and run2 where the latter supports propagating waves, while the former will generate evanescent wave solutions as oscillations at frequencies above the buoyancy frequency are not supported. Although the mode number, K, for run1 is subcritical for the lowest mode ($K > 1$) and the non-dimensional mountain height is sub-critical with respect to the typical mountain height of the domain, locally h_n exceeds the critical limit. The flow is then non-linear and goes through a "hydraulic transition" which is the case in run1 (Fig. 4a). In run1 the flow is partially blocked only behind the obstacles where the critical limit is exceeded, i.e. no discernible perturbations are seen in transects away from the "critical" obstacles. The model domain is centered at such a critical obstacle (Fig. 1, at $(x,y) \approx (200, 200)$) across which the section shown in Fig. 4 is extracted. In run2 and run3, on the other hand, propagating non-linear waves are seen and the drag on the flow is distributed throughout the entire domain, not confined to a few topographic features. Nevertheless, locally the drag exerted on the flow by the topography in run1 is significant and comparable in magnitude to run2 and run3. This is illustrated by showing the percent change of the horizontally averaged velocity with respect to the background velocity u_0 (Fig. 5). In run1 significant drag occurs near the depth corresponding to $Nz/u_0 = \pi$, and the average velocity is reduced by more than 20%. The largest decrease in relative velocity is due to flow blockage in run1, whereas in run2 and run3 the near-bottom reduction in relative velocity is due to bottom drag. Internal wave drag acts at run2, decreasing continuously with increasing height above bottom. For the more realistic N-profile of run3, the drag away from the bottom is concentrated at the pycnocline centered at a ~20 m thick layer around $Nz/u_0 = \pi$.

A proxy is calculated for the turbulent kinetic energy (TKE) by assuming that the cross-stream averages describe both the mean current and velocities associated with internal waves (Skyllingstad and Wijesekera, 2004). Computing the perturbations of u, v, and w by (for the u-component)

$$u' = u - \frac{1}{n_y}\sum_y u(x,y,z),$$ (11)

where n_y is the number of grid points in the cross-stream direction, an estimate of the turbulent kinetic energy is expressed by $TKE = 1/2(u'^2 + v'^2 + w'^2)$. The fields of TKE for run1, run2, and run3 are shown in Fig. 6, and support the inferences from percent-change velocity profiles (Fig. 5). In this representation, the cross-stream averaging of topography smooths out the large obstacles. The maximum reduction of the background flow due to drag induced by the internal gravity waves observed in run3 (Fig. 5c) is restricted to the stratified zone where the buoyancy frequency is large enough for the waves to break. This is also evident in the cross-stream averaged TKE from run3 (Fig. 6c) compared to run2 where high TKE (defined as TKE greater than the mean TKE level of run1) is present in 55% of the domain. The corresponding value for run1 and run3 is 28% and 14%, respectively. In run1, TKE is elevated closer to the bottom in the vicinity of large obstacles (not seen in the average topography), particularly behind the central obstacle. The difference between run1 and run2, and run3 is also evident in Fig. 7 where a horizontal section of TKE at a level corresponding to 95 m above the bottom topography is shown. The evanescent modes in run1 lead to weak perturbations in TKE away from the topography as well, but the perturbations in TKE are significantly greater for the breaking waves in run2 and run3 (the maximum TKE for run2 and run3 is 3 and 4 times greater, respectively, compared to run1). TKE integrated over the domain is 1.27×10^5 m^5 s^{-2}, 2.80×10^5 m^5 s^{-2}, and 0.71×10^5 m^5 s^{-2} for run1, run2, and run3, respectively, confirming run2 as the most turbulent. Run2 has the highest vertical mode number, and the non-dimensional obstacle heights of the major topographic features are well above the critical value. Blocked flow drag is expected at low levels and at several vertical levels due to waves, clearly visible in Figs. 4b and 5b.The maximum reduction in the velocity close to the topography is a combination of the blocked flow drag and the deepest wave.

5.2. Mixing

Given the open boundaries, the rate of change in the domain-integrated background potential energy cannot be used as a proxy for mixing. To diagnose the bulk measure for mixing a method suggested by Burchard and Rennau (2008) is adopted. For a
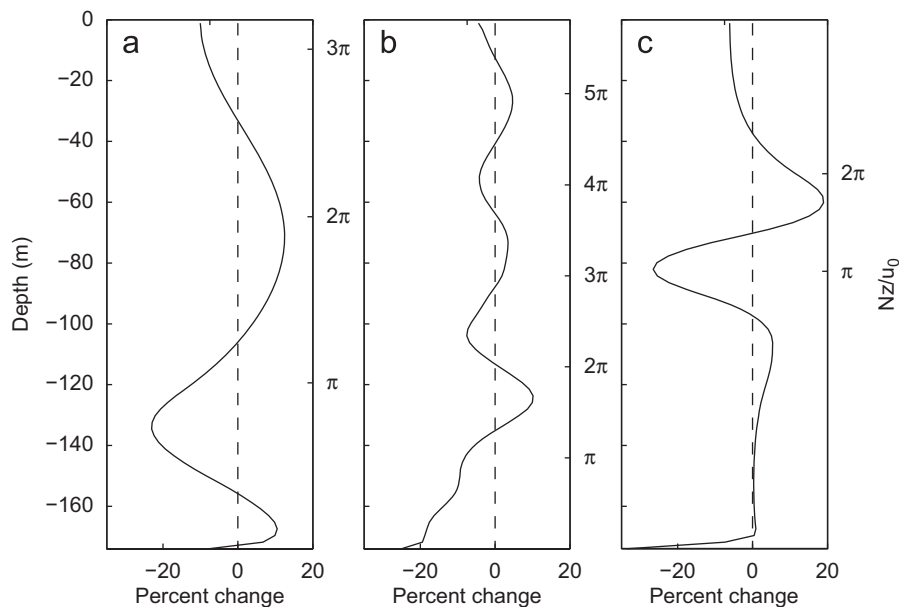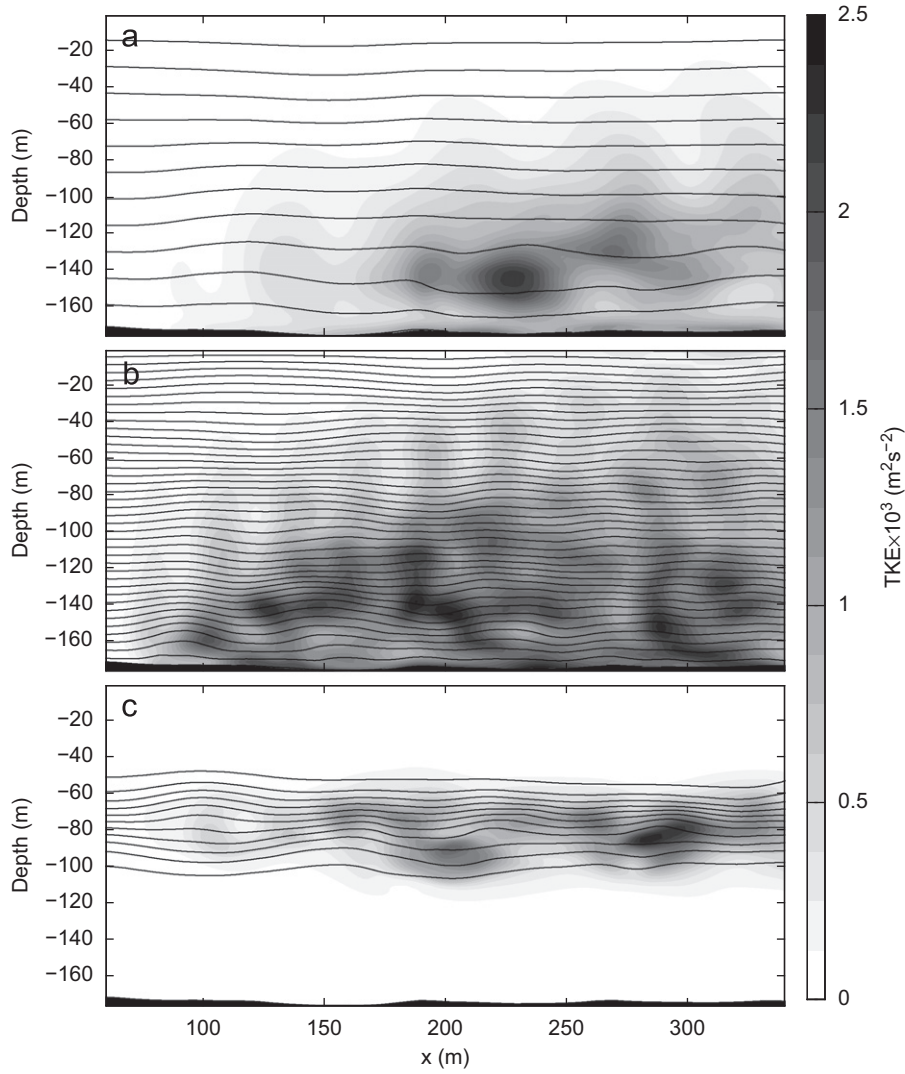

Fig. 5. Vertical profiles of the percent change of the horizontally domain- and time-averaged (8.5–10.5 h) u component of velocity relative to the background velocity u_0 for (a) run1, (b) run2, and (c) run3.

Fig. 6. Cross-stream average of potential density and TKE averaged in time between 8.5 and 10.5 h for (a) run1, (b) run2, and (c) run3.
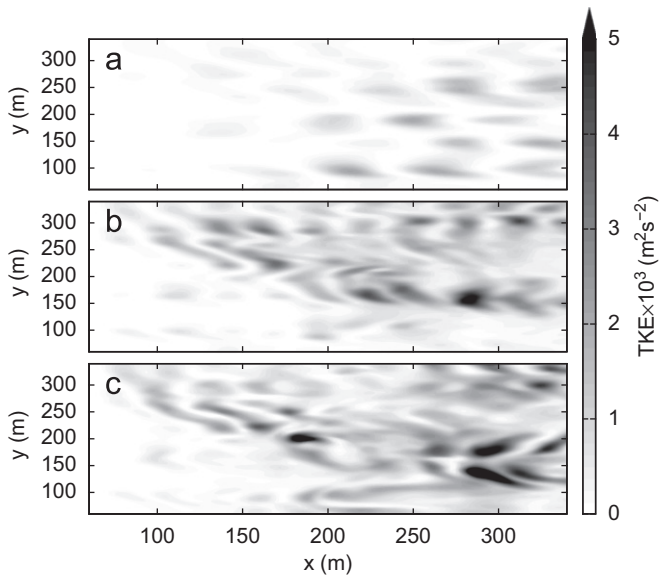

Fig. 7. Horizontal section of TKE at a height 95 m above the bottom, averaged in time between 8.5 and 10.5 h for (a) run1, (b) run2, and (c) run3.

conservative tracer s without any internal sources or sinks, a conservation equation for the square of the mean tracer is developed assuming that the turbulent fluxes can be parameterized as down-gradient fluxes with different diffusivities in the horizontal and in the vertical direction

$$\partial_t(s^2)+(v_j\partial_j)(s^2)-\partial_x(k_h\partial_x(s^2))-\partial_y(k_h\partial_y(s^2))-\partial_z(k_z\partial_z(s^2))$$
$$= -2k_h(\partial_x s)^2-2k_h(\partial_y s)^2-2k_z(\partial_z s)^2 \equiv -D^{phys}(s^2), \qquad (12)$$

where s is a tracer (in our case density), k_h and k_z are the horizontal and vertical turbulent diffusivities, and the spatial partial derivative is defined as $\partial_i=\partial/\partial_{x_i}$ with indices $i,j=1,2,3$ defining the spatial coordinates x_i ($x_1=x$, $x_2=y$ and $x_3=z$). The terms on the r.h.s. of Eq. (12) denote the turbulent mean tracer variance decay, D^{phys}, shown to be a suitable measure for mixing. Burchard and Rennau (2008) also present a method for quantifying the numerical mixing (due to the advection scheme) in ocean models by calculating the numerically induced tracer variance decay

$$D^{num}\{(s^n_{p,q,r})^2\}_{i,j,k}=\frac{A\{(s^n_{p,q,r})^2\}_{i,j,k}-(A\{s^n_{p,q,r}\}_{i,j,k})^2}{\Delta t}, \qquad (13)$$

where A is the advection operator of the numerical model and Δt is the model time step. D^{num} is quantified by diagnostically applying

the advection operator on the square of the tracer field and subtract the square of the advected tracer field for each time step. The resulting D^{phys} and D^{num} after applying these two methods on our results are presented in Fig. 8a–d. Strong tracer gradients and increased velocities associated with the internal waves induce numerical mixing orders of magnitude greater than the physical mixing in some locations (compare Fig. 4 with Fig. 8). This is consistent with the results of Rennau and Burchard (2009) for the Arkona Sea. The patches of high variance decay are always associated with negative (anti-diffusive) variance decay of the same magnitude. The former is an effect of the TVD scheme limiter ensuring monotonicity, and the latter is an effect of the non-monotone, higher-order (2nd order accurate) scheme. Similar behaviour is found by Burchard and Rennau (2008). The volume-integrated variance decay is -0.3×10^{-3} kg^2 m^{-3} s^{-1} and -5.9×10^{-3} kg^2 m^{-3} s^{-1} for run1 and run3, respectively. The negative values are due to the anti-diffusive properties of the superbee-limited (TVD) advection scheme. The volume-integrated physical mixing is 1.2×10^{-6} kg^2 m^{-3} s^{-1} and 3.4×10^{-6} kg^2 m^{-3} s^{-1}.

The vertical diffusivity associated with the numerical mixing can be estimated by $v_z^{num} = D^{num}/2(\partial_z s)^2$. As a result of the anti-diffusive D_{num}, the vertical numerical diffusivity has both negative and positive contributions presented separately in Fig. 8e–h, averaged in the cross-stream section along x. Horizontally averaged profiles are then presented for run1 and run3 (Fig. 9). The depth of the maximum vertical diffusivity is not necessarily co-located with the maximum variance decay due to the inverse dependence on the vertical tracer gradient. Particularly for run1, the maximum vertical diffusivity is associated with small $\partial_z s$, while the variance decay has maxima and minima where the velocity and gradients are large. Run3 has relatively enhanced numerical diffusivity compared to run1 (Figs. 8e–h and 10) with comparable contribution from the negative, anti-diffusive component. The distribution of positive and negative contributions to v_z^{num} is obtained by counting the number of occurrences in bins of v_z^{num} (Fig. 10). While the opposing contributions are evenly distributed in run1, run3 shows more frequent occurrences of negative diffusion, particularly in the range $10^{-3} < v_z^{num} < 10^{-2}$, which densely populates the domain.

5.3. Parameterization of topographic drag

Generally the drag exerted by the topography on the flow can be described by two conceptual models whose relevance depends on the non-dimensional obstacle height (Lott and Miller, 1997). In the atmospheric context of flow over mountains, when h_n is small the flow is forced over the mountain and the vertical motion of the fluid forces gravity waves. The surface stress due to these gravity waves has a magnitude given by Eq. (4) or similar expressions (Palmer et al., 1986; Kim and Arakawa, 1995; Lott and Miller, 1997). At large h_n, the vertical motion of the fluid is limited and the low level flow has to flow around the mountains, effectively reducing h in Eq. (4) and introducing a drag on the flow due to the blocked flow at low levels. Following Lott and Miller (1997), the depth of the blocked layer can be expressed as $z_b/h = \max[0,(h_n-h_{nc})/h_n]$, where h_{nc} is a critical non-dimensional mountain height of order unity. In this study $h_n < 1$ at low levels for all cases except run2, and the blocked flow drag has an insignificant contribution to the total drag on the flow, especially for the cases with a hyperbolic tangent density profile.
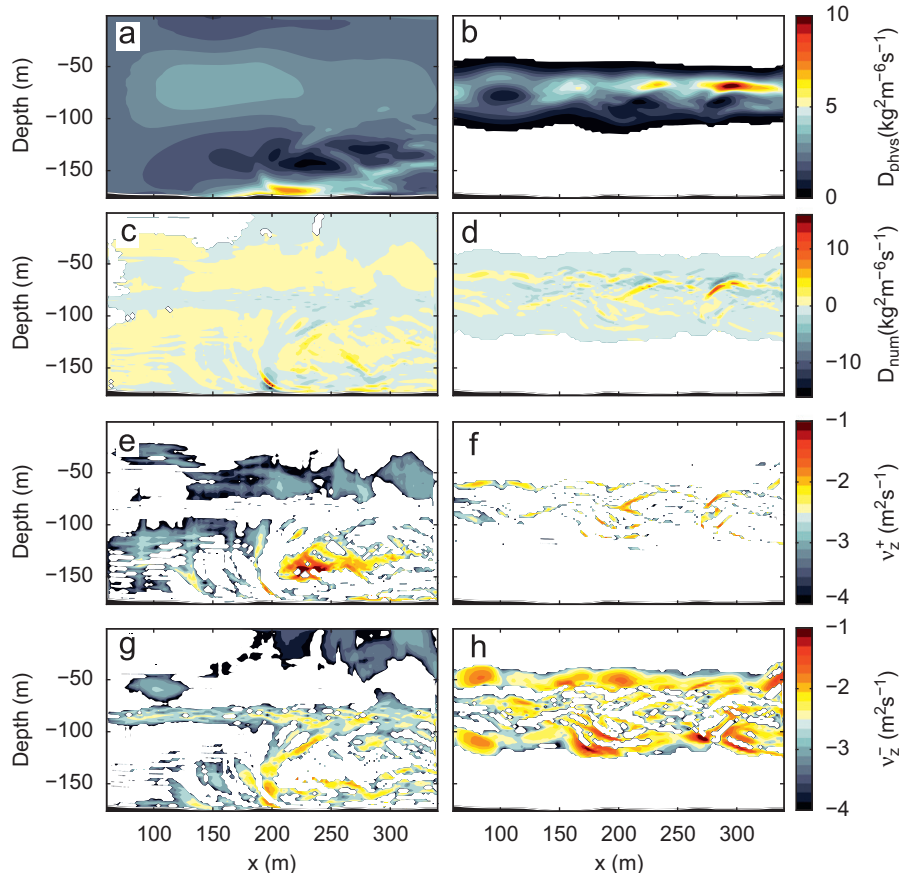

Fig. 8. (first column: run1; second column: run3) Physical mixing calculated according to Eq. (12) from (a) run1 ($10^{11} \times D_{phys}$) and (b) run3 ($10^{10} \times D_{phys}$), numerical mixing calculated according to Eq. (13) from (c) run1 ($10^7 \times D_{num}$) and (d) run3 ($10^6 \times D_{num}$), (e–f) positive and (g–h) negative numerical viscosity from run1 and run3, respectively. In (b) $10^{10} \times D_{phys} < 0.1$ is masked with white colour for clarity.
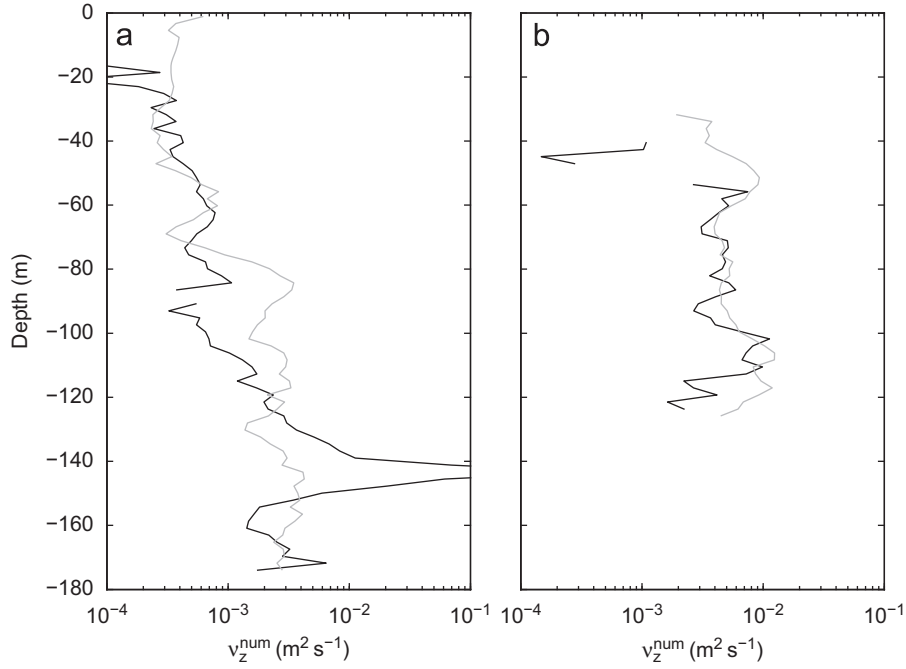
Fig. 9. Vertical profile of the vertical diffusivity from (a) run1 and (b) run3, calculated from the volume-averaged D_{num}, averaged in time between 8.5 and 10.5 h. Positive (black) and negative (gray) contributions are shown separately. One data point for run1 at ~ 145 m depth is off the scale with $\nu_z^{num} \sim 1$ m^2 s^{-1}.
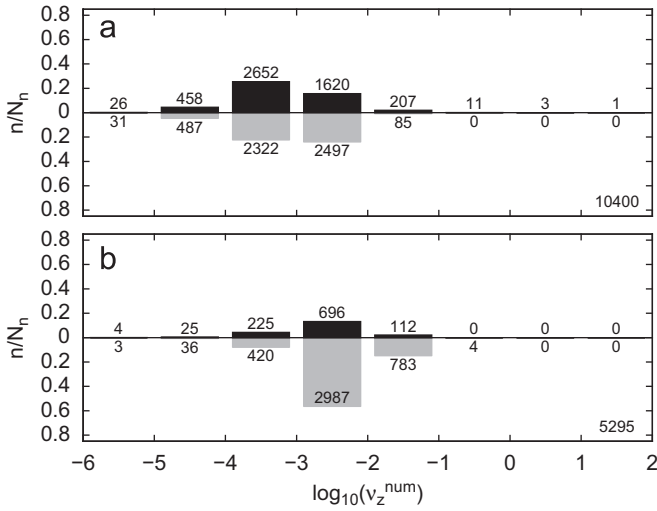

Fig. 10. Distribution of the cross-stream averaged numerical diffusivity by the number of grid cells, n, with positive diffusivity (black bars) and negative diffusivity (grey bars) relative to the total number of cells with non-zero diffusivity, N_n, for (a) run1 and (b) run3. The number of cells for each diffusivity level is denoted over each bar and N_n in the lower right corner.

We have also tested an additional case with drag due to the blocked flow parameterized following Lott and Miller (1997) and using the linear density profile of run2 such that $h_n > 1$ (not shown). This results in a blocked flow layer depth of approximately half the typical mountain height (6–7 m), and shows increased drag at the bottom and a well-mixed layer with a thickness on the order of z_b. Above the blocked layer, the magnitude of the gravity wave drag can be estimated from the vertical wave momentum flux, assuming linear, hydrostatic waves

$$\tau = -\rho_0 \overline{u'w'} = \frac{1}{2}\rho k U N \delta h^2, \qquad (14)$$

where the vertical wavenumber m is replaced by N/U (the hydrostatic dispersion relation is $m = N/U$ when $k^2 \ll m^2$, k being the

horizontal wavenumber). Depending on the horizontal wavenumber, evanescent $(k > N/U)$ or propagating $(k < N/U)$ wave solutions may be expected, but only the latter results in a pressure gradient over the topography and an associated drag force. Adding the wave drag Eq. (14) of all mountains within one grid point region (GPR) leads to Eq. (5). Using the high resolution topographic data we choose to express κ as a function of the statistical properties of the resolved topography following Lott and Miller (1997),

$$(\kappa_x, \kappa_y) = \frac{\sigma}{4\mu} G(B \cos^2 \theta + C \sin^2 \theta, (B-C) \sin \theta \cos \theta), \qquad (15)$$

where $B = 1 - 0.18\gamma - 0.04\gamma^2$, $C = 0.48\gamma + 0.3\gamma^2$, and the difference in the along stream and across stream wave stress is expressed in κ leading to κ_x and κ_y in the along and across stream direction, respectively. Applying the parameters obtained from Eqs. (8a)–(8d) we get $(\kappa_x, \kappa_y) = (0.02, 0.0004)$ m^{-1}.

For hydrostatic waves, their impact on the local static stability and shear may be combined to form a minimum local Richardson number (Ri_m) representing the smallest Richardson number Ri achieved under the influence of internal gravity waves

$$Ri_m = Ri \frac{1 - \frac{N}{U}\delta h}{\left(1 + Ri^{1/2}\frac{N}{U}\delta h\right)^2}. \qquad (16)$$

The presence of the waves may lead to local instability in a stable background flow either by a convective overturning mechanism (numerator of Eq. (16) becomes small) or by a billow instability mechanism (denominator of Eq. (16) becomes large) (Palmer et al., 1986). By defining a critical Ri (typically $Ri_c = 0.25$) and employing a saturation hypothesis (Lindzen, 1981), the vertical distribution of the gravity wave drag is estimated. When $Ri_m < Ri_c$, instability results in turbulent dissipation of the wave such that its amplitude is reduced until it regains stability. Below this critical level $\tau = \tau_s$, from the Eliassen–Palm theorem (Eliassen and Palm, 1961), for vertically propagating waves in the absence of transience and dissipation. If N is constant, the wave amplitude must increase with height as the density is reduced, until the

wave becomes unstable. In the case with a hyperbolic tangent profile, $N \approx 0$ at low levels; the minimum Richardson number formulation fails in the nearly neutral stratification at low levels. Consequently a simpler scheme is applied where the wave amplitude is assumed to be equal to the typical mountain height, $\delta h = h = 2\mu$, at low levels as $N \approx \partial\rho/\partial z \approx 0$, and wave breaking is assumed to commence at the level where δh equals the saturation wave amplitude given by $\delta h_{sat} = U/N$. From Eq. (16) this corresponds to the purely convective instability limit and is a strict requirement. Due to the low buoyancy frequency at low levels, however, attenuation of the wave amplitude with height (evanescent modes) may be expected and δh is probably overestimated.

We conduct two runs (run4 and run5) to test the topographic drag parameterization, each with the hyperbolic-tangent density profile and the Mellor and Yamada (1982) 2-1/2 level turbulence closure scheme (MY2.5). The only difference is that run4 employs the resolved topography, whereas run5 has flat bottom but includes the wave drag parameterization. Velocity and density distributions at $y=200$ m are contrasted in Fig. 11. As the Ri drops below the critical level (and even becomes negative by wave overturning, see Fig. 4c), the turbulence closure prohibits the overturning of waves by increasing the vertical diffusivity. This results in well-mixed neutrally stratified patches visible in Fig. 11a. Otherwise the results from run4 are qualitatively similar to run3 in both velocity and density distribution (compare Figs. 4c and 11a), and the cross-stream averaged TKE (compare Figs. 6c and 12a). The only difference between run3 and run4 is that run4 employs the MY2.5 closure whereas run3 does not. When applying the gravity wave parameterization (run5), the turbulence closure is retained as it smooths the strong velocity gradients imposed by the parameterization of the wave drag. Because the

domain resembles one GPR, a horizontally constant drag was applied throughout the domain, resulting in a smoother velocity structure (Fig. 11c). The estimation of TKE by subtracting the cross-stream averaged velocity is not a good approximation for run5. This is due to the lack of topography and the constant drag employed in run5 which results in TKE estimates two orders of magnitude smaller than run4 (Fig. 12b). Because there is no significant wave activity in run5, the TKE may be alternatively estimated by calculating the velocity fluctuations after removing the background velocity. This results in a domain-integrated TKE of 0.65×10^5 m^5 s^{-2} in better agreement with the resolved topography results (0.71×10^5 m^5 s^{-2} for run3 and 0.76×10^5 m^5 s^{-2} for run4). The similarity between run3 and run4 is confirmed by the percent change of the horizontally domain-averaged and time-averaged velocity relative to the background velocity (Fig. 13). In run5, although remarkably similar in the domain average TKE (equal to run3 within 14% and to run4 within 25%), the wave drag is deposited over a too shallow layer (5 m and 8 m shallower compared to run3 and run4, respectively) resulting in an overestimated drag (integrated over the domain) and consequently a larger reduction of the velocity (89% and 122% larger compared to run3 and run4) in the layer where the wave parameterization predicts wave breaking (Fig. 13c).

The volume-integrated variance decay of run4 and run5 is -4.3×10^{-3} kg^2 m^{-3} s^{-1} and -1.63×10^{-3} kg^2 m^{-3} s^{-1}, respectively. This is about 70% and 30% of run3, respectively, due to the smoother density fields in run4 and run5. In Fig. 14 the vertical profile of the diffusivity estimated from D_{num} is shown together with the vertical eddy diffusivity from the turbulence closure. The eddy diffusivity from the turbulence closure is more than two times greater than the numerical diffusivities. Fig. 14
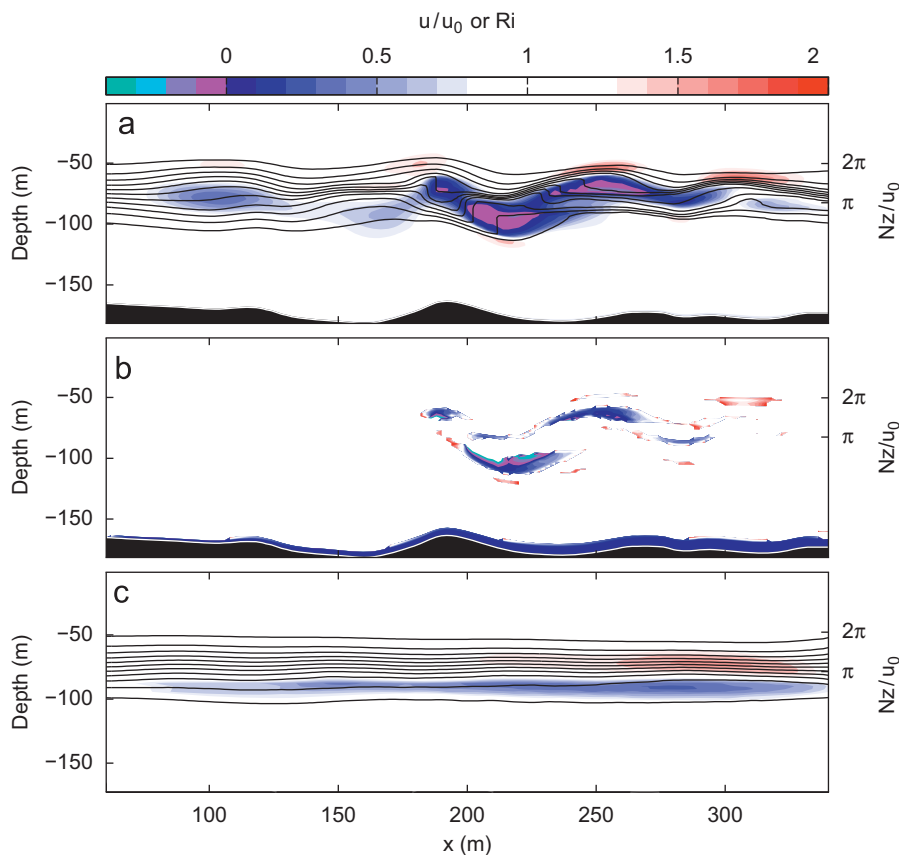

Fig. 11. Vertical cross section of potential density and the horizontal velocity normalized by u_0 for (a) run4 and (c) run5 at $y=200$ m averaged over the period from approximately 8.5 to 10.5 h. Density contours are drawn at 0.05 kg m^{-3} intervals. In (b) the Richardson number (Ri) is shown for run4. $Ri > 2$ is not shown for clarity.
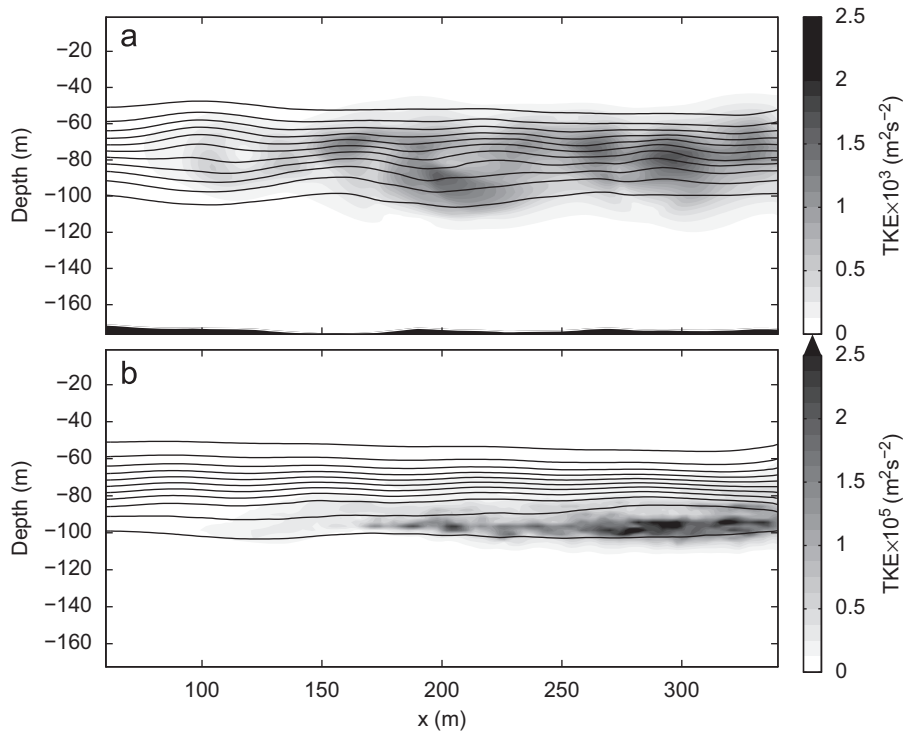
Fig. 12. Cross-stream average of potential density and TKE averaged in time between 8.5 and 10.5 h for (a) run4 and (b) run5.
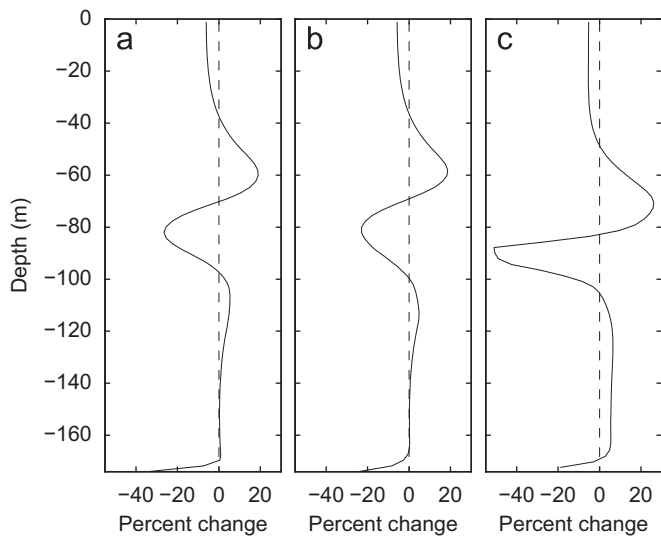

Fig. 13. Vertical profile of the percent change of the horizontally domain averaged and time averaged (8.5–10.5 h) u component of velocity relative to the background velocity u_0 for (a) run3, (b) run4, and (c) run5.

Fig. 14. Vertical profile of the vertical diffusivity from run4 calculated from a horizontally averaged D_{num} time averaged over the period from 8.5 to 10.5 h and the vertical diffusivity from the turbulence closure (grey).

also illustrates that the positive and negative contributions from the numerical mixing, due to the superbee limited TVD advection scheme, are of the same order of magnitude. The zero numerical diffusivity near the bottom and toward the surface in run4 (and run3) is due to the vanishing vertical density gradient. The volume-integrated D_{phys} for run4 is 3.3×10^{-6} kg^2 m^{-3} s^{-1}, equal to that in run3 (3.4×10^{-6} kg^2 m^{-3} s^{-1}) to within 3%, while for run5, using the internal gravity wave parameterization, the volume-integrated D_{phys} is 4.0×10^{-6} kg^2 m^{-3} s^{-1}, i.e. 20% larger. This suggests that, although the parameterization is underestimating the local internal wave drag (Fig. 11c), the total mixing due to the internal waves is captured satisfactory by the parameterization.
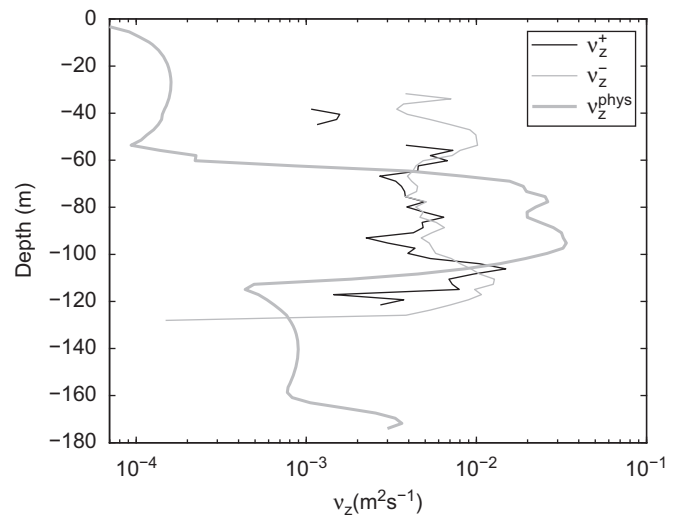
6. Concluding remarks

Recent observations of the dense, bottom-attached plume of the Faroe Bank Channel overflow show that in the O(100) m thick stratified interface between the mixed bottom layer and the overlaying ambient, in addition to the entrainment and shear-induced mixing, breaking internal waves can contribute to vertical mixing (Fer et al., 2010; Seim and Fer, 2011). Regional model simulations using local turbulence closure schemes did not capture this (Seim et al., 2010). Here, we suggest that internal wave drag and internal wave breaking in response to flow over complex topography can be responsible for elevated levels of mixing at the stratified interface. Numerical simulations of stratified flow over complex topography

have been performed using a high-resolution, non-hydrostatic ocean model, to study the drag exerted on the flow by bottom obstacles. Several runs with various stratification but with realistic topography are discussed. Depending on the stratification, the drag on the flow is described by three different processes, acting separately or in combination; internal wave drag, blocked flow drag, and hydraulic drag. Three cases with a hyperbolic tangent density profile, resembling the well mixed bottom layer and the stratified interface of the Faroe Bank Channel overflow, were performed to illustrate the possible interfacial mixing caused by rough bottom topography. The simulations support the hypothesis that the complex bottom topography leads to wave overturning and significant mixing in the stratified interface. The drag exerted on the flow as internal waves break reduces the horizontally domain averaged velocity by up to 27% in the stratified interface, imposing a strong shear on the flow. Typical topographic irregularities of order 10 m height present in the domain are common in nature; the non-dimensional obstacle height, h_n, is typically less than unity in the domain and only locally exceeds the critical limit. Complex flow structures, however, result extending far above the bottom contributing to mixing at levels about 10 times the obstacle heights where the stratified interface is located.

When the stratification is linear, the buoyancy frequency N is constant, we contrasted two cases where N was approximately doubled. For the weak stratification case significant disturbances in the flow were observed only locally near the critical obstacles, leading to blocked flow drag. In stronger stratification propagating internal waves lead to complex flow structures, internal wave breaking, and mixing, distributing the drag on the flow in the entire water column. The domain integrated mixing is significantly increased in the latter case compared to the weak stratification case. All rest set equal, imposing the realistic density profile representative of the Faroe Bank Channel overflow increased the volume integrated physical mixing by a factor of three above the weakly stratified case.

A parameterization of the wave drag when the sub-grid-scale topography statistical properties are available was applied in a final simulation where a flat bottom is prescribed. The internal wave drag parameterization, tested on the hyperbolic tangent case, yields reasonable levels of turbulent kinetic energy and predicts wave breaking at the correct level compared to the simulation with resolved topography. The vertical extent of the layer where the wave breaking is effective, however, is underestimated, leading to an overestimated volume-integrated wave drag (i.e. larger reduction in velocity) in the layer. Volume integrated physical mixing is satisfactorily captured by the parameterization yielding values about 20% larger than the case with the realistic topography. When the sub-grid scale topography is unknown caution should be exerted when tuning such a parameterization, but in areas where strong interaction between the flow and topography is expected, such as the Faroe Bank Channel overflow area, parameterizations of the internal wave drag may be applied to improve the results of models too coarse to resolve the internal wave drag or where high resolution topographic data is lacking.

Acknowledgements

References

Baines, P.G., 1979. Observations of stratified flow over two-dimensional obstacles in fluid of finite depth. Tellus 31, 351–371.

Baines, P.G., 1995. Topographic Effects in Stratified Flows. Cambridge Monographs on Mechanics. Cambridge University Press.

Berntsen, H., Kowalik, Z., Sælid, S., Sørli, K., 1981. Efficient numerical simulation of ocean hydrodynamics by a splitting procedure. Modeling, Identification and Control 2, 181–199.

Berntsen, J., 2000. Users Guide for a Modesplit σ-Coordinate Numerical Ocean Model. Technical Report 135, Department of Applied Mathematics, University of Bergen, Johs. Bruns gt.12, N-5008 Bergen, Norway. 48p.

Berntsen, J., Xing, J., Davies, A.M., 2009. Numerical studies of flow over a sill: sensitivity of the non-hydrostatic effects to the grid size. Ocean Dynamics 59, 1043–1059.

Blumberg, A.F., Mellor, G.L., 1987. A description of a three-dimensional coastal ocean circulation model. In: Heaps, N. (Ed.), Three-Dimensional Coastal Ocean Models. Coastal and Estuarine Series, vol. 4. , American Geophysical Union, pp. 1–16.

Burchard, H., Rennau, H., 2008. Comparative quantification of physically and numerically induced mixing in ocean models. Ocean Modelling 20, 293–311.

Eliassen, A., Palm, E., 1961. On the transfer of energy in stationary mountain waves. Geophysics Publications 22 (3), 1–23.

Fer, I., Voet, G., Seim, K.S., Rudels, B., Latarius, K., 2010. Intense mixing of the Faroe bank channel overflow. Geophysical Research Letters 37, L02604. doi:10.1029/2009GL041924.

Gregg, M.C., 1987. Diapycnal mixing in the thermocline: a review. Journal of Geophysical Research 92 (C5), 5249–5286.

Hove, J., 2003. Statistical Properties of the Sea Bottom in the Ormen Lange Area. Technical Report 3, UNIFOB, Bergen Center of Computational Science, Computational Mathematics Unit.

Huppert, H.E., Miles, J.W., 1969. Lee waves in a stratified flow. Part 3. Semi-elliptical obstacle. Journal of Fluid Mechanics 55, 481–496.

Kim, Y.-J., Arakawa, A., 1995. Improvement of orographic gravity wave parameterization using a mesoscale gravity wave model. Journal of the Atmospheric Sciences 52, 1875–1902.

Klymak, J.M., Legg, S.M., 2010. A simple mixing scheme for models that resolve breaking internal waves. Ocean Modelling 33, 224–234.

Kowalik, Z., Murty, T.S., 1993. Numerical Modeling of Ocean Dynamics. Advanced Series on Ocean Engineering, vol. 5. , World Scientific.

Lamb, K.G., 1994. Numerical experiments of internal wave generation by strong tidal flow across a finite amplitude bank edge. Journal of Geophysical Research 99, 843–864.

Ledwell, J.R., Montgomery, E., Polzin, K.L., Laurant, L.C.S., Toole, J., 2000. Evidence for enhanced mixing over rough topography in the Abyssal ocean. Nature 403, 179–182.

Lindzen, R.S., 1981. Turbulence and stress owing to gravity wave and tidal breakdown. Journal of Geophysical Research 86 (C10), 9707–9714.

Long, R.R., 1955. Some aspects of the flow of stratified fluids. III. Continuous density gradients. Tellus 7, 341–357.

Lott, F., Miller, M.J., 1997. A new subgrid-scale orographic drag parametrization: its formulation and testing. Quarterly Journal of the Royal Meteorological Society 123, 101–127.

Martinsen, E.A., Engedahl, H., 1987. Implementation and testing of a lateral boundary scheme as an open boundary condition in a barotropic ocean model. Coastal Engineering 11, 603–627.

Mellor, G.L., 1996. Users Guide for a Three-Dimensional, Primitive Equation, Numerical Ocean Model. Technical Report. Princeton University.

Mellor, G.L., Yamada, T., 1982. Development of a turbulence closure model for geophysical fluid problems. Reviews of Geophysics and Space Physics 20, 851–875.

Molemaker, M.J., McWilliams, J.C., 2010. Local balance and cross-scale flux of available potential energy. Journal of Fluid Mechanics 645, 295–314.

Palmer, T.N., Shutts, G.J., Swinebank, R., 1986. Allevation of a systematic westerly bias in circulation and numerical weather prediction models through an orographic gravity-wave drag parameterization. Quarterly Journal of the Royal Meteorological Society 112, 1001–1039.

Peters, H., Johns, W.E., 2005. Mixing and entrainment in the red sea outflow plume. Part II. Turbulence characteristics. Journal of Physical Oceanography 35, 584–600.

Polzin, K.L., Toole, J.M., Ledwell, J.R., Schmitt, R.W., 1997. Spatial variability of turbulent mixing in the Abyssal ocean. Science 276, 93–96.

Rennau, H., Burchard, H., 2009. Quantitative analysis of numerically induced mixing in a costal model application. Ocean Dynamics 59, 671–687.

Seim, K.S., Fer, I., 2011. Mixing in the stratified interface of the Faroe bank channel overflow: the role of transverse circulation and internal waves. Journal of Geophysical Research 116, C07022.

Seim, K.S., Fer, I., Berntsen, J., 2010. Regional simulations of the Faroe bank channel overflow using a σ-coordinate ocean model. Ocean Modelling 35, 31–44.

Skyllingstad, E.D., Wijesekera, H.W., 2004. Large-eddy simulation of flow over two-dimensional obstacles: high drag states and mixing. Journal of Physical Oceanography 34, 94–112.

Thurnherr, A.M., 2006. Diapycnal mixing associated with an overflow in a deep submarine canyon. Deep-Sea Research II 53, 194–206.

Winters, K.B., Lombard, P.N., Riley, J.J., D'Asaro, E.A., 1995. Available potential energy and mixing in density-stratified fluids. Journal of Fluid Mechanics 289, 115–128.

Xing, J., Davies, A., 2006. Processes influencing tidal mixing in the region of sills. Geophysical Research Letters 33, L04603. doi:10.1029/2005GL025226.

Xing, J., Davies, A.M., 2011. Tidal mixing in sill regions: influence of sill depth and aspect ratio. Ocean Dynamics 61, 1697–1717.

Yang, H.Q., Przekwas, A.J., 1992. A comparative study of advanced shock-capturing schemes applied to Burgers equation. Journal of Computational Physics 102, 139–159.